Springer

Journal of Mechanical Science and Technology 22 (2008) 2590~2599

Journal of Mechanical Science and Technology

www.springerlink.com/content/1738-494x
DOI 10.1007/s12206-008-0905-8

Numerical study of droplet motion in a microchannel with different contact angles †

Jiyoung Choi and Gihun Son*

Department of Mechanical Engineering, Sogang University, Seoul, 121-742, Korea

(Manuscript Received May 2, 2008; Revised September 3, 2008; Accepted September 4, 2008)

Abstract

The droplet motion in a microchannel with different contact angles, which is applicable to a typical proton exchange membrane fuel cell (PEMFC), was studied numerically by solving the equations governing the conservation of mass and momentum. The gas-liquid interface or droplet shape was determined by a level set method which was modified to treat the static and dynamic contact angles. The matching conditions at the interface were accurately imposed by incorporating the ghost fluid approach based on a sharp-interface representation. Based on the numerical results, the droplet dynamics including the sliding and detachment of droplets was found to depend significantly on the contact angle. Also, the effects of inlet flow velocity, droplet size and side wall on the droplet motion were investigated.

Keywords: Contact angle; Droplet motion; Level set method; Microchannel

1. Introduction

Two-phase flow in a microchannel has received attentions for various engineering applications, such as PEMFCs, micro cooling devices and biomedical instruments. In this work, we focus on the air-water two-phase flow in a gas channel of a PEMFC. It is directly related to the water management problem, which is essentially important for the performance of a PEMFC. Despite a number of studies, the dynamics of water droplets in a microchannel is still not well understood. Recently, numerical simulations for further clarifying the droplet dynamics have been performed.

Quan et al. [1] simulated the transport of water droplets and films in an air flow channel of a PEMFC using the volume-of-fluid (VOF) method implemented in the FLUENT. In the VOF method, the gas-liquid interface is tracked by the VOF function representing the volume fraction of a particular phase in each cell. Their results show that the bend area of a U-shaped channel affects significantly the deformation and distribution of water droplets and films. Subsequently, Quan and Lai [2] included the effect of contact angle in their numerical analysis of water management in the air flow channel. In the VOF method, which requires the determination (or reconstruction) of the interface configuration from the volume fraction function, the contact angle condition is not directly imposed on the wall but is used to adjust the interface curvature near the wall. Their study indicates that the hydrophilicity of channel surface is an important factor in water transport.

Cai et al. [3] also studied the mobility of water droplets in a hydrophilic or hydrophobic microchannel using the VOF method. They found that the removal of water on a hydrophobic surface is faster than that on a hydrophilic surface, and a combination of a hydrophilic side wall with a hydrophobic bottom wall can avoid water accumulation on the bottom surface.

Theodorakakos et al. [4] investigated the detachment process of water droplets from solid surfaces. Incorporating a more general contact angle model, to

† This paper was recommended for publication in revised form by Associate Editor Haecheon Choi

*Corresponding author. Tel.: +82 2 705 8641, Fax.: +82 2 712 0799
E-mail address: gihun@sogang.ac.kr

Account for the dynamic change between advancing and receding contact angles during droplet motion, into the VOF method, they predicted the droplet detachment process from different channel surfaces. However, the dynamic contact angle model is not straightforward to properly implement in the VOF method, which requires quite complicated geometric calculations to reconstruct the interface configurations satisfying the variable contact angle condition as well as the volume fraction.

Very recently, Mukherjee and Kandlikar [5] conducted a numerical analysis of the growth and departure of a water droplet in an air flow channel by using the level set (LS) method [6]. In the method, the LS function is defined as a signed distance from the interface and is used for tracking the gas-liquid interface. Since the distance function and its spatial derivatives are smooth and continuous, the LS method can be used to compute an interface curvature more accurately than the VOF method using a step function. Their method is based on diffuse-interface modeling, in which the interface is treated as a transition region smoothed over several grid spacings. Their simulations were limited to the spreading motion of a droplet before departing from the surface.

In this study, numerical simulations are performed to further clarify the droplet motion in a microchannel. The droplet shape is determined by the LS method which is modified to treat the static and dynamic contact angles. The matching conditions at the interface are accurately imposed by incorporating the ghost fluid approach based on a sharp-interface representation [7-10]. The effects of contact angle, inlet flow velocity and droplet size on the droplet motion are investigated. The interaction between droplets is also included in the analysis.

2. Numerical analysis

The numerical approach is based on the LS formulation modified by Son and Dhir [10] for a sharp-interface representation. Fig. 1 shows the computational domain used in this study. The gas-liquid interface is tracked by the LS function ϕ, which is defined as a signed distance from the interface. The equations governing the conservation of mass and momentum for the gas-liquid region can be written as

$$\nabla \cdot \mathbf{u} = 0 \tag{1}$$

$$\rho \frac{D\mathbf{u}}{Dt} = -\nabla p + \rho \mathbf{g} - \sigma \kappa \nabla \alpha_\phi + \nabla \cdot \mu [\nabla \mathbf{u} + (\nabla \mathbf{u})^T] \tag{2}$$

where

$$\begin{aligned} \frac{D}{Dt} &= \frac{\partial}{\partial t} + \mathbf{u} \cdot \nabla \\ \kappa &= \nabla \cdot (\nabla \phi / |\nabla \phi|) \\ \alpha_\phi &= 1 \quad \text{if } \phi > 0 \\ &= 0 \quad \text{if } \phi \le 0 \\ \rho &= \rho_g (1 - F_\phi) + \rho_l F_\phi \\ \mu^{-1} &= \mu_g^{-1} (1 - F_\phi) + \mu_l^{-1} F_\phi \end{aligned}$$

Here, α_ϕ is the discontinuous step function and the interface curvature κ is evaluated by the smooth LS function. The effective density ρ and viscosity μ are evaluated from a fraction function F_ϕ, which is defined as

$$\begin{aligned} F_\phi &= 1 \quad \text{if } \alpha_\phi(\phi_A) = \alpha_\phi(\phi_B) = 1 \\ &= 0 \quad \text{if } \alpha_\phi(\phi_A) = \alpha_\phi(\phi_B) = 0 \\ &= \frac{\max(\phi_A, \phi_B)}{\max(\phi_A, \phi_B) - \min(\phi_A, \phi_B)} \quad \text{otherwise} \end{aligned}$$

where the subscripts "A" and "B" denote the grid points adjacent to the location where F_ϕ is evaluated, as described in the references [9, 10].

In the level set formulation, the LS function ϕ is advanced and reinitialized as

$$\frac{D\phi}{Dt} = 0 \tag{3}$$

$$\frac{\partial \phi}{\partial \tau} = S(\phi_o)(1 - |\nabla \phi|) \tag{4}$$

where

$$\begin{aligned} S(\phi_o) &= 0 \quad \text{if } |\phi_o| \le d_\varepsilon \\ &= \frac{\phi_o}{\sqrt{\phi_o^2 + h^2}} \quad \text{otherwise} \end{aligned} \tag{5}$$

Here h is a grid spacing, ϕ_o is a solution of Eq. (3), and d_ε is the distance between the interface and the nearest grid point, as depicted in [11]. This formulation of the sign function improves the mass-conservation property of LS method significantly [11].

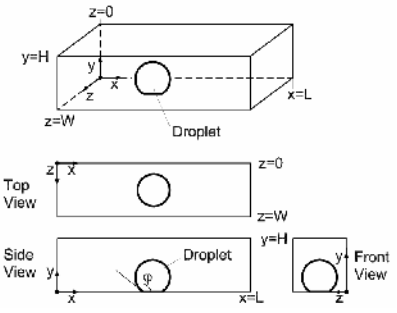

Fig. 1. Computational domain.

To preserve mass conservation from any numerical errors, the following volume-correction step is added to the level set formulation:

$$\frac{\partial \phi}{\partial \tau} = (V_{lo} - V_l)\left|\nabla \phi\right| \tag{6}$$

where V_{lo} is the liquid volume that satisfies mass conservation and V_l is a liquid volume evaluated form the computed LS function ϕ. The liquid volume loss $(V_{lo} - V_l)$ is corrected by adjusting ϕ from Eq. (6).

The governing equations are spatially discretized on a staggered grid system in which the velocity components are defined at cell faces whereas the other dependent variables at cell centers. A second-order essentially nonoscillatory (ENO) scheme is used for the convection terms and the distance function and a second-order central difference scheme for the other terms. While the governing equations are discretized temporally, the convection and source terms are treated by a first-order explicit scheme and the diffusion terms by a fully implicit scheme. During the computations, the time step Δt is chosen to prevent the possible numerical instability caused by the CFL condition and surface tension, as described in [9]:

$$\Delta t < 0.5 \min\left(\frac{h}{|\mathbf{u}|}, \sqrt{\frac{\rho_l h^3}{8\pi\sigma}} \right)$$

The boundary conditions used in this study are as follows (refer to Fig. 1):
at the inlet ($x = 0$),

$$u = u_{in}, \quad v = w = 0, \quad \frac{\partial \phi}{\partial x} = 0 \tag{7}$$

at the outlet ($x = L$),

$$p = 0, \quad \frac{\partial \mathbf{u}}{\partial x} = \frac{\partial \phi}{\partial x} = 0 \tag{8}$$

at the wall (y =0, H or z =0, W),

$$\mathbf{u} = 0, \quad \mathbf{n}_w \cdot \nabla \phi = \cos\varphi \tag{9}$$

In Eq. (9), a contact angle φ, formed on the gas-liquid-solid interline (or contact line), is used to evaluate the LS function at the wall. For real surfaces where the contact angle varies dynamically between an advancing contact angle φ_a and a receding contact angle φ_r, a dynamic contact model proposed by Fukai et al. [12] is implemented in the LS method, as done in our previous study [13]. As long as the contact angle changes in the range of $\varphi_r < \varphi < \varphi_a$, the contact line does not move. However, while the contact line moves, the contact angle remains constant as $\varphi = \varphi_a$ or $\varphi = \varphi_r$. This contact angle condition is not easy to implement in the VOF method, especially for $\varphi_r < \varphi < \varphi_a$, in which case the interface reconstruction from the VOF function has to be made with the interface-wall contact line fixed. Its implementation into the LS method is straightforward as follows:

1. Assume $(\partial\phi/\partial t) = 0$ at the wall, which means that the contact line is stationary, and then evaluate a contact angle from Eq. (9), $\varphi = \cos^{-1}[\mathbf{n}_w \cdot \nabla\phi]$.
2. If $\varphi_r \le \varphi \le \varphi_a$, no further calculation is required because the contact line is stationary as assumed in step 1. Otherwise, set $\varphi = \max\{\varphi_r, \min(\varphi_a, \varphi)\}$ since $\varphi = \varphi_r$ or $\varphi = \varphi_a$ while the contact line moves.
3. Update ϕ from Eq. (9).

To prevent the droplet from escaping out of the computational domain and to perform the computation until the droplet motion attains a steady state, the domain is moved with droplet sliding velocity *U*. In this case, *D*/*Dt* is rewritten as

$$\frac{D}{Dt} = \frac{\partial}{\partial t} + (\mathbf{u} - U\mathbf{i}) \cdot \nabla$$

where the droplet sliding velocity in the x-direction is obtained from the condition that the droplet should be located at a specified position X_l of the moving computational domain. Eq. (3) is decomposed into two fractional steps:

$$\frac{\phi^* - \phi^n}{\Delta t} + (\mathbf{u} - U^n\mathbf{i}) \cdot \nabla\phi^n = 0 \tag{10}$$

$$\frac{\phi^{n+1} - \phi^*}{\Delta t} - (U^{n+1} - U^n)\mathbf{i} \cdot \nabla\phi^* = 0 \tag{11}$$

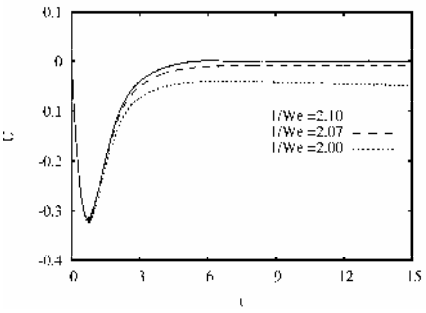

Fig. 2. Droplet sliding velocities for different Weber numbers (*We*).

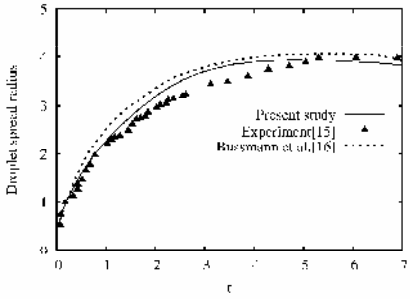

Fig. 3. Comparison of temporal variations of droplet spread radius.

where

$$U^{n+1} = U^n + \frac{X_l^* - X_l}{\Delta t} \quad \text{and} \quad X_l^* = \frac{\int x\alpha(\phi^*)dV}{\int \alpha(\phi^*)dV}$$

3. Results and discussion

In presenting numerical results including figures, all the dimensional variables are nondimensionalized by a reference length l_o, a reference velocity u_o, and their combination. The reference scales are determined from the characteristics of each problem. Also, the following dimensionless parameters are defined:

$$\mathrm{Re} = \frac{\rho_l u_o l_o}{\mu_l} \qquad We = \frac{\rho_l u_o^2 l_o}{\sigma}$$

First, to validate the LS formulation including a dynamic contact angle model, the computations are made for a droplet adhering to a vertical wall. We choose the x-coordinate in the direction opposite to that of the gravitational vector. For an ideal surface with $\varphi_a = \varphi_r$, droplets of all sizes slide along the vertical surface. For a non-ideal surface with $\varphi_a \neq \varphi_r$, the droplet maintains attached to the vertical surface

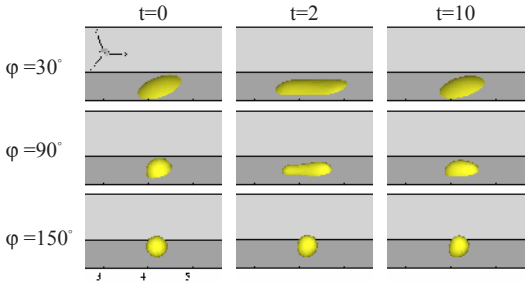

Fig. 4. Effect of contact angle on droplet motion for u_{in}=3 and V_d=0.0335.

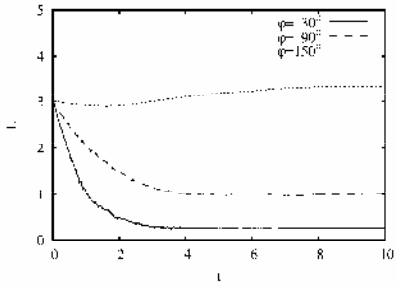

Fig. 5. Effect of contact angle on droplet sliding velocity for u_{in}=3 and V_d=0.0335.

or slide down, depending on the droplet size, contact angle hysteresis and surface tension. To make the governing equations dimensionless, the droplet radius is chosen for l_o and $\sqrt{gl_o}$ for u_o. In the calculations, we use $\mathrm{Re} = 10$, $\rho_g / \rho_l = 10^{-3}$, $\mu_g / \mu_l = 10^{-2}$, $\varphi_a = 90^\circ$, $\varphi_r = 60^\circ$ and different values of We. The computational domain is taken as a hexahedral cell 6 × 3 × 6. Initially a hemispherical droplet with a radius of 1 is placed on a vertical surface. The calculation is carried out until the droplet sliding velocity attains an asymptotic value. The results are plotted in Fig. 2. When the surface tension coefficient (or $1/We$) is small, the surface tension force cannot be balanced with the gravitational force and hence the droplet slides down. However, for $1/We \geq 2.10$, the droplet becomes stationary. The critical value of We for the droplet slide differs by less than 1% when compared with the result obtained by Dimitrakopoulos and Higdon [14] using a spectral boundary-element method.

The LS formulation is also tested for droplet impact on a horizontal surface. The droplet radius is used for l_o and the impact velocity for u_o. Based on the experiment of Chandra and Avedisian [15] for heptane droplets falling on a steel plate, we chose $\mathrm{Re} = 1.22 \times 10^3$, $We = 21$, $\rho_g / \rho_l = 1.76 \times 10^{-3}$, $\mu_g / \mu_l = 4.56 \times 10^{-2}$, $\varphi_a = \varphi_r = 32^\circ$. The computation

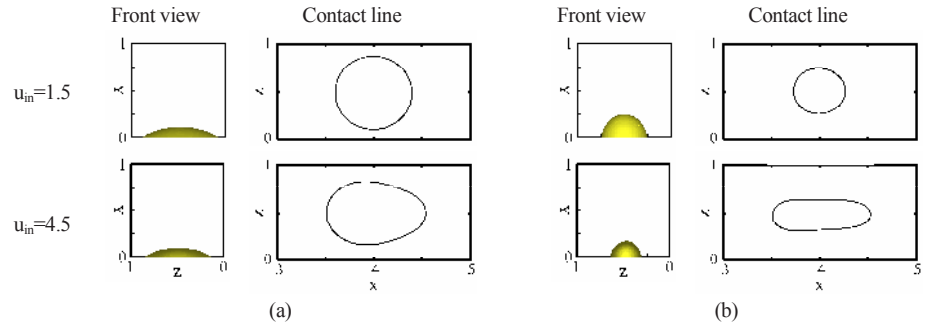

Fig. 6. Steady-state droplet shapes for different inlet flow velocities and contact angles: (a) φ=30° and (b) φ =90°.

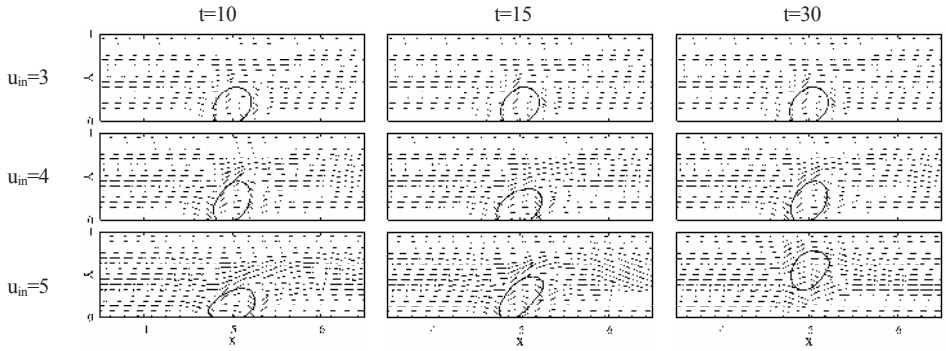

Fig. 7. Effect of inlet flow velocity on the droplet shape and velocity field at z=0.5 for φ=150°.

is made in an axisymmetric computational domain of 5.12 × 5.12. Fig. 3 shows the temporal variation of droplet spread radius. The present result is more comparable to the experiment data [15] than the numerical result of Bussmann et al. [16] using the VOF method.

Now, the computations are performed for droplet motion in a microchannel. The effect of gravity is neglected for this case. The governing equations are nondimensionalized by l_o = 1mm and u_o = 1m/s, which are of the same order as channel size and inlet air velocity used in the previous studies on PEMFCs [1-4]. The computational domain is depicted in Fig. 1. The parameters used in the calculations are $\mathrm{Re} = 10^3$, $We = 13.7$, $\rho_g / \rho_l = 1.2 \times 10^{-3}$, $\mu_g / \mu_l = 1.78 \times 10^{-2}$. The channel has a cross-section of 1×1 and a length of 8. During the computations, we use $h = 3.125 \times 10^{-2}$ and $\Delta t = 10^{-3}$. In this study, the computations are made to investigate the effects of contact angle, inlet air flow velocity, droplet size and side wall on the droplet motion. As the base case, we choose an air inlet velocity of u_{in} = 3, a droplet volume of V_d = 0.0335 and the location of a droplet of x=4 and z=0.5. Three different contact angles of φ =30°, 90°, and 150° are used.

Fig. 4 shows the effect of contact angle on the droplet motion. The initial shape of a droplet in each case is taken to be a truncated sphere that satisfies a specified contact angle at the gas-liquid-solid interline while keeping its volume constant. For φ =30°, the droplet initially elongates due to the interfacial drag and then it returns to nearly the original shape due to the restoring force of surface tension. At steady state ($t \geq 10$), the droplet-wall contact area decreases as the contact angle increases. The droplet sliding velocities for different contact angles are plotted in Fig. 5. As the droplet-wall contact area decreases with contact angle, the droplet velocity increases. This indicates that a hydrophobic surface with a high contact angle is more effective for water removal than a hydrophilic surface with a low contact angle.

To investigate the effect of inlet air flow velocity, simulations are performed for u_{in} = 1.5 and 4.5. In Fig. 6, the droplet shapes at steady state for φ =30° and φ =90° are plotted with different air inlet velocities. When the inlet velocity is 1.5, the droplet moves along the flow direction with slight change in its shape. As the air velocity increases, the droplet shape be-

comes oblate ellipsoidal from spherical and the droplet-wall contact area increases. Table 1 lists the steady-state velocities and contact areas of sliding droplets with different contact angles and air velocities. It is found that the droplet-wall contact area increases as the air inlet velocity increases. For φ=30°, the ratio of the droplet sliding velocity to the air inlet velocity, U/u_{in}, increases with the air inlet velocity. However, it decreases for a higher contact angle of φ=90°, in which case the increase in the contact area with u_{in} is pronounced.

Figs. 7 and 8 show the effect of air velocity on droplet motion when the contact angle is increased up to φ=150°. As the air velocity increases, a wake region

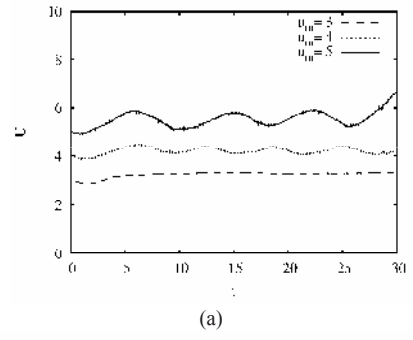

Fig. 8. Effect of inlet flow velocity on droplet motion for φ=150°: (a) droplet sliding velocity and (b) droplet-wall contact area.

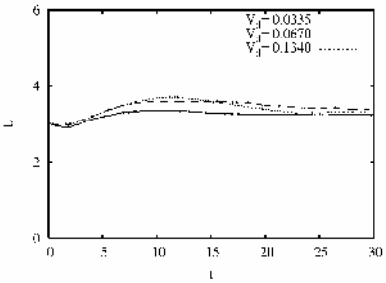

Fig. 9. Effect of droplet volume on droplet sliding velocity for u_{in}=3 and φ=150°.

Table 1. Steady-state velocities and contact areas of sliding droplets with different contact angles and inlet flow velocities.

	u_{in}	U	U/ u_{in}	Contact area
30°	1.5	0.092	0.061	0.556
	3.0	0.263	0.088	0.564
	4.5	0.476	0.106	0.608
90°	1.5	0.524	0.349	0.202
	3.0	1.017	0.339	0.235
	4.5	1.230	0.273	0.283

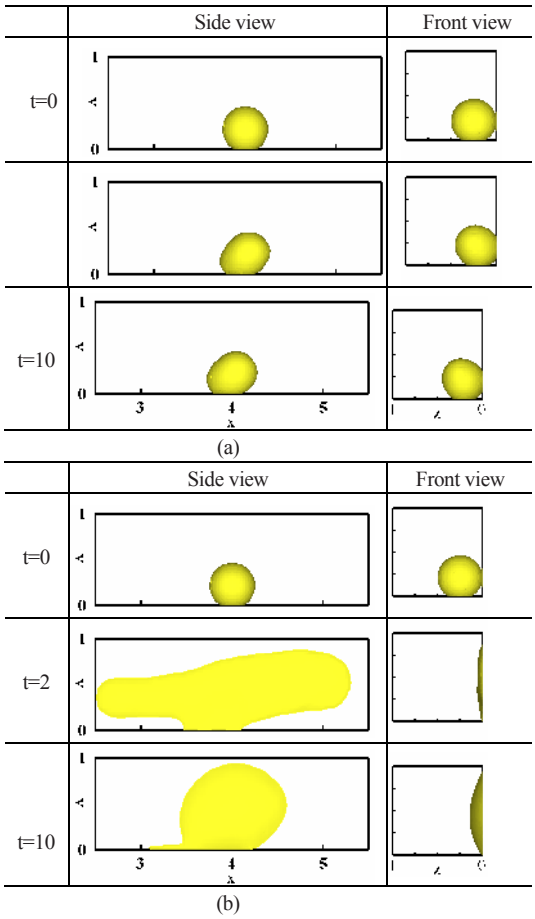

Fig. 10. Droplet motion near the channel corner with φ_B=150° at the bottom wall and different contact angles at the side wall: (a) φ_S=150° and (b) φ_S=30°.

formed behind the droplet is expanded, as plotted in Fig. 7. This causes the droplet motion to be unstable. At u_{in} = 4, the droplet sliding velocity and the droplet-wall contact area start to oscillate due to imbalance between the drag and surface tension forces. The oscillation amplitude increases with u_{in}. When the air velocity is increased to 5, the droplet detaches from the bottom wall and rises away from the surface. The

droplet departing from the wall has a higher velocity as it is injected into the relatively faster air stream.

The effect of droplet size on the droplet motion is studied through the computations with $V_d = 0.0335$, 0.067 and 0.134. The results are plotted in Fig. 9. As the droplet volume increases, the droplet base in contact with the bottom wall elongates and increases. The dependency of droplet size on the sliding velocity of a droplet is found to be weak.

Simulations are performed for the droplet motion when a droplet touches the side wall as well as the bottom wall. Fig. 10 presents the effect of φ_S, the contact angle at the side wall, on the droplet motion while keeping φ_B constant. For $\varphi_S = 150^\circ$, the droplet slides without large spreading. Its sliding velocity at steady state is 2.25, which is much smaller than 3.23 for the droplet in contact with only the bottom wall. When φ_S is decreased up to 30°, the droplet spreads up along the side wall rapidly. This is due to the up- ward component of surface tension force acting on the droplet-wall contact line. As the droplet spread area on the side wall increases, the terminal sliding velocity of a droplet decreases to 0.24. When the droplet gets to a steady state at t=10, it has no contact with the bottom wall. Therefore, the combination of a hydrophilic side wall and a hydrophobic bottom wall is an effective way for the removal of water droplets from the bottom wall, which is assumed to be a gas diffusion layer of a PEMFC.

The effect of contact angle hysteresis ($\varphi_a \neq \varphi_r$) or dynamic contact angle ($\varphi_r \leq \varphi \leq \varphi_a$) on the droplet shape is plotted in Fig. 11. In the calculations, we use $\varphi_a = 150^\circ$ and $\varphi_r = 60^\circ$. The initial shape of droplet is taken to be a hemisphere with $\varphi = 90^\circ$. For $u_{in} < 2.5$, the droplet remains stationary on the surface because the surface tension force is dominant. In this case, the contact angle around the droplet-wall contact line is adjusted between φ_a and φ_r so that the net force in the horizontal direction is zero. As the air inlet velocity increases, the droplet begins to move. For $u_{in} = 2.5$ and 3.0, the droplet sliding velocities are 0.69 and 0.72, respectively.

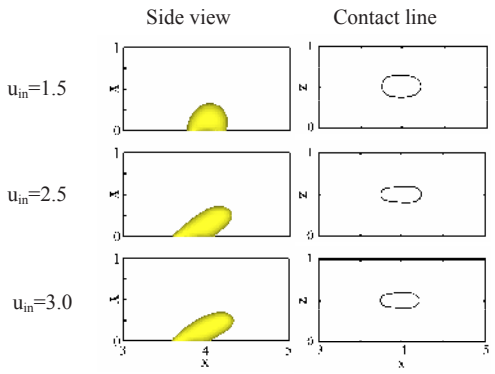

Fig. 11. Steady-state droplet shapes with dynamic contact angle of $60^o \leq \varphi \leq 150^o$ and different inlet flow velocities.

Fig. 12 presents the dependence of droplet motion on a receding contact angle while keeping $\varphi_a = 150^\circ$. As the receding contact angle increases, the droplet-wall contact area decreases and the droplet sliding velocity increases. For $\varphi_r = 60^\circ$, 90° and 120°, the droplet sliding velocities are 0.72, 1.72 and 2.43, respectively.

The effect of advancing contact angle on the droplet motion for $\varphi_r = 60^\circ$ is plotted in Fig. 13. The droplet sliding velocity is 0.64 for $\varphi_a = 60^\circ$, but the droplet

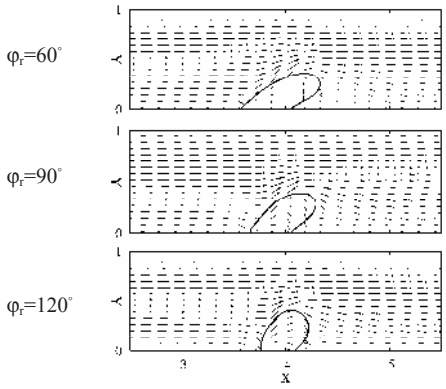

Fig. 12. Effect of receding contact angle on the steady-state droplet shape and velocity field at z=0.5 for φ_a=150°, u_{in}=3 and V_d=0.0335.

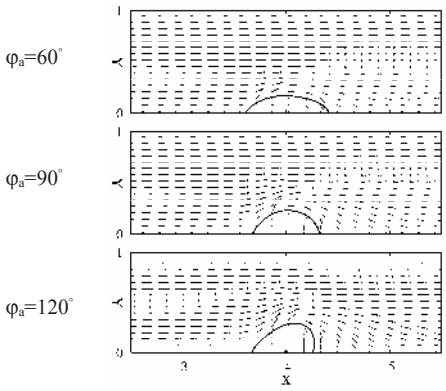

Fig. 13. Effect of advancing contact angle on the steady-state droplet shape and velocity field at z=0.5 for φ_r=150°, u_{in}=3 and V_d=0.0335.

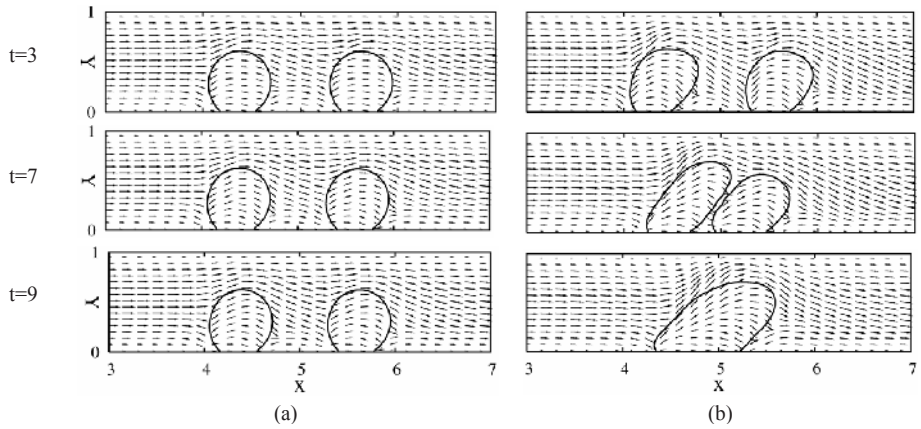

Fig. 14. Droplet-droplet interaction and the associated velocity field at z=0.5 for φ=150°, V_d=0.134 and different inlet velocities: (a) u_{in}=1.5 and (b) u_{in}=3.0.

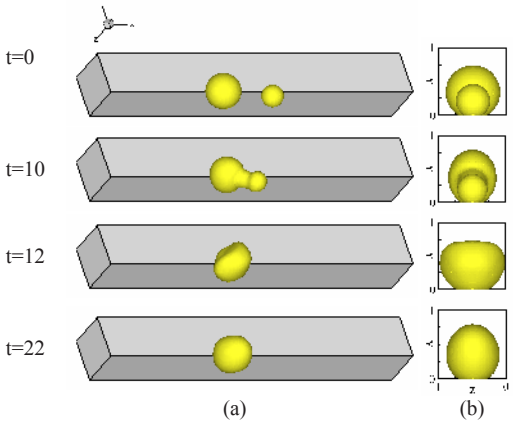

Fig. 15. Droplet merging pattern for φ_B=150° and φ_S=φ_T=150°: (a) three-dimensional view and (b) front view.

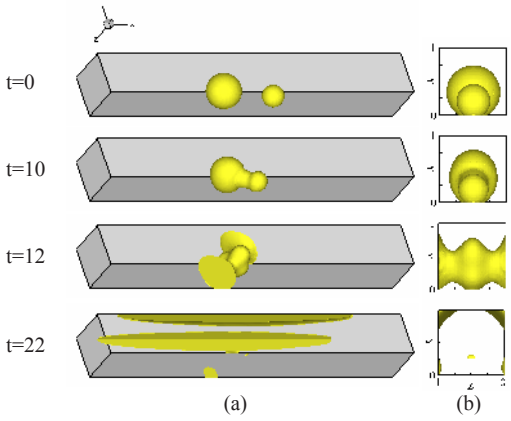

Fig. 16. Droplet merging pattern for φ_B=150° and φ_S=φ_T=30°: (a) three-dimensional view and (b) front view.

remains stationary for $\varphi_a \geq 90^\circ$. It is interesting to note that the droplet slides slowly when the contact area decreases with the advancing contact angle. This is caused by the fact that the wake region behind a droplet is expanded as the advancing contact angle increases, as seen in Fig. 13. Therefore the droplet sliding velocity increases as the contact angle increases and the contact angle hysteresis ($\varphi_a - \varphi_r$) decreases.

A computation is performed to investigate the interaction between droplets in a microchannel. For this case, we use a longer channel of *L=10* and a contact angle of 150° at all the walls. Initially a droplet is placed at x=4.4 and another droplet at x=5.6. Each droplet has the same volume of $V_d = 0.134$. Fig. 14 shows the interaction between droplets for different inlet velocities. For $u_{in} = 1.5$, the velocity field near the downstream droplet has insignificant difference from that near the upstream droplet. This causes the droplet shape and sliding velocity to be nearly identical for both the upstream and downstream droplets. When the inlet velocity is increased to 3.0, droplets evolve as demonstrated in Fig. 14(b). The wake region behind the upstream droplet is expanded with the increase in inlet velocity. As the drag force on the downstream droplet is reduced, the distance between two droplets becomes shorter with time. This results in large deformation of the upstream as well as downstream droplets and then merging of the droplets.

Fig. 15 shows another droplet merging pattern in a microchannel. Initially a droplet with $V_d = 0.268$ is placed at x=4.4 and another droplet with $V_d = 0.067$

at x=5.6. We use $u_{in} = 1.5$ and $\varphi_B = \varphi_S = 150^\circ$. When the locations of the two droplets are reversed, the droplets do not merge. After the two droplets merge, the elongated merged droplet springs back quickly due to the restoring force of surface tension. Thereafter, the merged droplet oscillates on the bottom wall and then attains a steady state, as seen at t=22.

Fig. 16 shows the droplet merging pattern when the contact angles of the side and top walls are reduced to $\varphi = 30^\circ$. After the two droplets merge, the merged droplet climbs up the side wall and then spreads on the top wall. As the droplet evolves with time, liquid films form near the channel corner between the top and side walls. A comparison of Figs. 15 and 16 indicates that the hydrophilic side wall helps to reduce the cross-section area occupied by water droplets which blocks the air flow.

4. Conclusions

The droplet motion in a microchannel has been investigated numerically by using the level set method to track the droplet shape, which is modified to treat the static and dynamic contact angles and further improved by employing a sharp-interface technique to accurately impose the matching conditions at the interface.

Computations were performed until the droplet motion attained a steady state by using the computational domain moving with the droplet sliding velocity. Based on the numerical results, the droplet sliding velocity was observed to increase as the contact angle increased and the contact angle hysteresis decreased. It was also found that the droplet detachment from the wall and the droplet merging process occurred when the wake region formed behind a droplet was pronounced with the increase in the inlet flow velocity and the contact angle.

As the inlet flow velocity increased, the droplet-wall contact area increased. At a low contact angle, the ratio of the droplet sliding velocity to the inlet flow velocity increased with the inlet flow velocity, but its dependency was the reverse at a higher contact angle. The effect of droplet size on the droplet sliding velocity was found to be weak.

A combination of a hydrophobic bottom wall and a hydrophilic side wall was demonstrated to be effective for water removal. It was also observed from the numerical simulations of droplet merging process that a hydrophilic side wall helps to reduce the cross-section area occupied by water droplets.

Acknowledgment

This work was supported by the Special Research Grant of Sogang University.

Nomenclature

g	:	Gravity
h	:	Grid spacing
H	:	Height of a microchannel
$\mathbf{i}$	:	Unit vector in the x-direction
l_o	:	Reference length
L	:	Length of a microchannel
$\mathbf{n}$	:	Unit normal vector
$\mathbf{n}_w$	:	Unit normal vector pointing into the wall
p	:	Pressure
R	:	Droplet radius
Re	:	Reynolds number
S	:	Sign function
t	:	Time
$\mathbf{u}$	:	Flow velocity vector, (u, v, w)
u_o	:	Reference velocity
U	:	Sliding velocity of a droplet
V	:	Volume
V_d	:	Volume of a droplet
W	:	Width of a microchannel
We	:	Weber number
x, y, z	:	Cartesian coordinate

Greek symbols

α_ϕ	:	Step function
κ	:	Interface curvature
μ	:	Dynamic viscosity
ρ	:	Density
σ	:	Surface tension coefficient
τ	:	Artificial time
ϕ	:	Distance function from the gas-liquid interface
φ	:	Contact angle

Subscripts

a, r	:	Advancing, receding
B, T, S	:	Bottom wall, top wall, side wall
g, l	:	Gas, liquid
in	:	Inlet

References

[1] P. Quan, B. Zhou, A. Sobiesiak and Z. S. Liu, Water behavior in serpentine micro-channel for proton exchange membrane fuel cell cathode, *J. Power Sources,* 152 (2005) 131-145.

[2] P. Quan and M. C. Lai, Numerical study of water management in the air flow channel of a PEM fuel cell cathode, *J. Power Sources,* 164 (2007) 222-237.

[3] Y. H. Cai, J. Hu, H. P. Ma, B. L. Ui and H. M. Zhang, Effects of hydrophilic/ hydrophobic properties on the water behavior in the micro-channels of a proton exchange membrane fuel cell, *J. Power Sources*, 161 (2006) 843-848.

[4] A. Theodorakakos, T. Ous, M. Gavaises, J. M. Nouri, N. Nikolopoulos and H. Yanagihara, Dynamics of water droplets detached from porous surfaces of relevance to PEM fuel cells, *J. Colloid Interf. Sci.*, 300 (2006) 673-687.

[5] A. Mukherkee and S. G. Kandlikar, A numerical analysis of growing water droplet inside an air supply channel of a PEM fuel cell, *Proc. 2006 ASME International Mechanical Engineering Congress and Exposition*, Chicago, IMECE 2006-14807.

[6] M. Sussman, P. Smereka and S. Osher, Level set approach for computing solutions to incompressible two-phase flow, *J. Comput. Phys.,* 114 (1994) 146-159.

[7] R. P. Fedkiw, T. Aslam, B. Merriman and S. Osher, A non-oscillatory Eulerian approach to interfaces in multimaterial flows (the ghost fluid method), *J. Comput. Phys.,* 152 (1999) 457-492.

[8] F. Gibou, R. P. Fedkiw, L. T. Cheng and M. Kang, A second-order-accurate symmetric discretization of the Poisson equation on irregular domains, *J. Comput. Phys.,* 15 (2000) 323-360.

[9] M. Sussman, K. M. Smith, M. Y. Hussaini, M. Ohta and R. Zhi-Wei, A sharp interface method for incompressible two-phase flows, *J. Comput. Phys.,* 221 (2007) 469-505.

[10] G. Son and V. K. Dhir, A level set method for analysis of film boiling on an immersed solid surface, *Numer. Heat Transfer B,* 52 (2007) 153-177.

[11] G. Son, A level set method for incompressible two-phase flows with immersed solid boundaries, *Numer. Heat Transfer B,* 47 (2005) 473-489.

[12] J. Fukai, Y. Shiiba, T. Yamamoto, O. Miyatake, O. Poulikakos, C. M. Megaridis and Z. Zhao, Wetting effects on the spreading of a liquid droplet colliding with a flat surface, *Phys. Fluids*, 7 (1995) 236-247.

[13] W. Lee and G. Son, Bubble dynamics and heat transfer during nucleate boiling in a microchannel, *Numer. Heat Transfer A*, 53 (2008) 1074-1090.

[14] P. Dimitrakopoulos and J. J. L. Higdon, On the gravitational displacement of three dimensional fluid droplets from inclined solid surfaces, *J. Fluid Mech.*, 395 (1999) 181-209.

[15] S. Chandra and C. T. Avedisian, On the collision of a droplet with a solid surface, *Proc. R. Soc. Lond. A*, 432 (1991) 13-41.

[16] M. Bussmann, S. Chandra and J. Mostaghimi, Modeling the splash of a droplet impacting a solid surface, *Phys. Fluids*, 12 (2000) 3121-3132.

Gihun Son received a B.S. and M.S. degree in Mechanical Engineering from Seoul National University in 1986 and 1988, respectively. He then went on to receive his Ph.D. degrees from UCLA in 1996. Dr. Son is currently a Professor of Mechanical Engineering at Sogang University in Seoul, Korea. Dr. Son's research interests are in the area of multiphase dynamics, heat transfer, and power system simulation.

Jiyoung Choi received a B.S. degree in Mechanical Engineering from Sogang University in 2005. He is a graduate student of Mechanical Engineering at Sogang University in Seoul, Korea. Choi's research interests are in the area of PEM fuel cell and microfluidics.